



**HAL**  
open science

## Transport in multiscale porous extrudates

A. Morgado Lopes, V. Wernert, Loic Sorbier, Vincent Lecocq, Mickaël Antoni,  
R. Denoyel

► **To cite this version:**

A. Morgado Lopes, V. Wernert, Loic Sorbier, Vincent Lecocq, Mickaël Antoni, et al.. Transport in multiscale porous extrudates. *Microporous and Mesoporous Materials*, 2021, 310, pp.110640. 10.1016/j.micromeso.2020.110640 . hal-03105512

**HAL Id: hal-03105512**

**<https://ifp.hal.science/hal-03105512>**

Submitted on 11 Jan 2021

**HAL** is a multi-disciplinary open access archive for the deposit and dissemination of scientific research documents, whether they are published or not. The documents may come from teaching and research institutions in France or abroad, or from public or private research centers.

L'archive ouverte pluridisciplinaire **HAL**, est destinée au dépôt et à la diffusion de documents scientifiques de niveau recherche, publiés ou non, émanant des établissements d'enseignement et de recherche français ou étrangers, des laboratoires publics ou privés.

# Transport in multiscale porous extrudates

A. Morgado Lopes<sup>a,b</sup>, V. Wernert<sup>a,\*</sup>, L. Sorbier<sup>b</sup>, V. Lecocq<sup>b</sup>, M. Antoni<sup>a</sup>, R. Denoyel<sup>a</sup>

<sup>a</sup>Aix-Marseille Université, CNRS, MADIREL, UMR 7246, Centre Saint-Jérôme, F-13397, Marseille cedex 20, France

<sup>b</sup>IFP Energies nouvelles, Rond-point de l'échangeur de Solaize, BP 3, 69360 Solaize, France

\*Corresponding author: Dr. Véronique Wernert, [veronique.wernert@univ-amu.fr](mailto:veronique.wernert@univ-amu.fr)

## Abstract

When considering porous materials that are shaped under a specific form for a given application, a possible anisotropy of structure, that could be created by the synthesis procedure, have to be considered. This anisotropy may have consequences, as observed here, on the transport properties. To evidence such anisotropy, several methods are proposed here in the case of extrudates of alumina used as catalysts supports. The simplest one seems to be the release of probes, here a salt, in controlled geometry. Electrical measurements are also simple in principle but limited to aqueous solutions and also to pore size ranges where the double layer can be screened. NMR is a very powerful tool, but the porous domain that is analyzed is always questionable. Finally, approaches such as band spreading analysis of chromatographic peak are also interesting in their ability to explore various pore domains by changing probe size, but a modeling is needed and the preparation of adapted column is sometimes itself a difficult task. The tortuosity of the material, analysed here in longitudinal and transverse directions, is used as an intercomparing parameter.

## 1. Introduction

The study of the topological properties of porous networks has long been of interest in many areas, not least of which in the catalysis sector. The accurate prediction of molecule behavior within catalysts is paramount in the development of efficient and profitable industrial processes. One specific and very well documented example is hydrotreatment within petroleum refineries [1,2]. While optimization is essential at every possible scale, the microscopic behavior of molecules within catalyst porous networks provides researchers with intricate challenges to this day. One such challenge is the complete description of the multifaceted behavior of large and complex molecules within such constrained systems. To this end, the porous system itself must be characterized in detail [3,4]. In addition to standard material structure parameters such as specific surface area, pore size distribution or porosity [5], tortuosity is a commonly used parameter which describes, at once, the entire spectrum of possible factors which might delay molecules along their path through a porous system [6]. Tortuosity should be an inherent property of the material; however, it is commonly overlooked because difficult to determine, which might lead to an underestimation of this parameter's predictive capabilities. Moreover, in most experimental procedures, only an apparent tortuosity is obtained that depends both on the probe used to determine it and on the phenomenon under study. Tortuosity is generally deduced from real transport experiments, but recent approaches use 3D reconstruction based on TEM, SEM or XRD imaging followed by a simulation of the transport such as random walk simulations, for instance [7,8,9]. In the case of reconstructed media, geometrical tortuosity may also be defined as a ratio of lengths of different pathways with and without porous medium, but this is less common in material science because the choice of the pathways is not clear. In this paper, only the ratio of a transport parameter with and without porous medium will be considered: this cover both experimental approaches and simulations in reconstructed media. In the case of tortuosity measurements based on conductivity, permeability or diffusion, it can be shown that it is equivalent to a ratio of distances to the square [6]. The apparent tortuosity determined experimentally depends on the probe size and its interaction with walls. Theoretically, tortuosity obtained with small probes having no specific interaction with walls could be considered as "absolute" and should be independent of the method. This is why electric (eq.1) and diffusional (eq.2) definitions of tortuosity are both applicable and accurate when it comes to determining the overall tortuosity of a material, though experimental procedures for diffusional methods require strictly non-adsorbing conditions and electrical methods require a full screening of surface effects.

$$\frac{\sigma^{eff}}{\sigma^0} = \frac{\varepsilon}{\tau} \quad (1)$$

$$\frac{D^{eff}}{D^0} = \frac{\varepsilon}{\tau} \quad (2)$$

The ratios of effective conductivity,  $\sigma^{eff}$ , versus bulk conductivity,  $\sigma^0$ , along with effective diffusion,  $D^{eff}$ , versus bulk diffusion,  $D^0$ , are analogous and both are a function of the porosity  $\varepsilon$  of the material where each property occurs, as delayed by a factor defined as the topological tortuosity,  $\tau$ . In special situations such as pulsed-field gradient nuclear magnetic resonance (PFG-NMR) experiments the porous volume term may be omitted to account for the fact that in these situations, the diffusion ratio is being calculated from the point of view of a molecule that is already within the porous network [10] leading to equation (3):

$$\frac{D^{eff}}{D^0} = \frac{1}{\tau} \quad (3)$$

Experimental details aside, these equations have proven successful at determining the topological tortuosity of different materials throughout the literature [6], with a good agreement between the two types of measurement in many cases [11,12]. Excepted the dilution method of suspension that can be used to determine the tortuosity of porous particles, preferentially spherical [13], other methods for measuring the tortuosity of porous materials usually involve their transformation into small layers (membranes) that can be set-up in permeation and diffusion cell experiments. The quantification of the tortuosity parameter seems particularly lacking in extruded or pellet supports despite a few attempts by NMR [14,15,16], that lead to very different values. PFG-NMR can be performed with small molecules however the tortuosity value obtained is usually confined to the micro-mesopore scale [15]. This is because the mesoporous volume, in general, contains most of the surface area in the material, as well as due to its larger contribution to the delay in percolation. The smaller cross-section and consequent lack of flow within mesopores severely constrains probes (to a greater degree with increasing molecular weight), causing diffusion to be a limiting step. Moreover, when considering the diffusion length of molecules during NMR experiment, they are often of the same magnitude of macropores size, when in the micrometer range, which make the diffusion coefficient measured in these domains apparently very close to that of the bulk [14]. Likewise, the orientation of the measurement is not often considered as only a one-dimensional field gradient is applied. This is especially pernicious when considering long anisotropic extrudates often used in reactor beds. A focus on the longitudinal diffusion will be informative but will neglect the main direction of percolation, given the much larger exchange surface area of the sides of the extrudate compared to the ends. If monoliths were anisotropic, transport could differ considerably depending on the direction in which the molecules are traversing the porous network. For extrudates, the process from they are obtained (extrusion) leads to macroporous channels that are oriented along the longitudinal axis, greatly enhancing the transport properties in that direction, because air or solvent bubbles are deformed by shear in the direction of extrusion [17]. In practice, whether in fixed bed,

bubbling or other reactor types, extrudates are usually submerged in the fluid phase, meaning molecular transport inwards and outwards from the extrudate occurs in all directions.

In this article, a complement approach to porous volume and pore size distribution experiments is proposed, with information on the pore organization and insight into the potential diffusional properties of molecules within the extrudate matrix in various orientations. A transport experiment based on chromatography in non-adsorbing conditions is first realized where band spreading is analyzed. Then the tortuosity of extrudates is determined by three different methods. The first one is based on the conductivity determination of an extrudate impregnated with a concentrated electrolyte. The second one is based on the determination of the diffusion coefficient of toluene by PFG-NMR. The third one is based on the determination of salt diffusion in extrudates by using a release method. The first and the third method easily enable measurements in longitudinal and lateral direction, whereas NMR was only used in the longitudinal configuration. In the following, the methods are first presented with the models that are applied. Then results obtained by the different methods are compared.

## **2. Experimental methods**

### **2.1. Alumina extrudates characterization and preparation**

The alumina porous extrudates were manufactured using the sol-gel method. The gel sample is retrieved after synthesis by precipitation of the aluminium salts, washed, dried and sieved. The monoliths are then subjected to additional kneading and extrusion processes before calcination at 700 °C. The kneading process involves the mixing of the gel inside rotating jaws which slightly alters its structure, narrowing its mesopore size distribution. The final extrudates have a cylindrical shape with an average radius of 0.94 mm. They have been characterized by gas adsorption manometry and mercury porosimetry. Nitrogen adsorption at 77K was performed with a Micromeritics ASAP2010 apparatus. Before analysis, the sample was evacuated at 150°C during 8h at pressure lower than 1Pa. Samples were analysed by intrusion-extrusion of mercury using Poremaster apparatus from Quantachrome. Two cycles of intrusion-extrusion were performed to check that measurements are done in a capillary regime and that no sample damaging occurs.

Extrudates were imaged by a EasyTom 150-160 CT-scanner (RX Solutions). Radios were taken at 160 kV, with a Varian detector of 3072×1944 pixels, with 1 µm pixel size. Volume were reconstructed from 1800 radios covering a full 360° rotation of the sample using filtered back-projection. Longitudinal and transversal slices were extracted from the reconstructed volume. For SEM analysis, extrudates were embedded in a poly-methyl-methacrylate resin (Aldrich) in longitudinal and transversal position and

mechanically polished with SiC papers. Polished sections were covered by a conductive carbon layer. Sections were imaged with a Supra 40 SEM (Zeiss), operating at 10 kV in backscattered electrons mode.

Alumina monoliths are too fragile to be extruded at sizes much larger than 2 cm and even at those sizes, the alumina paste has an occasional tendency to coil as it is extruded, resulting in curved extrudates. For NMR, straight extrudates were selected in order to enter the tube. For electrical measurements, chromatography, or diffusion release experiments straight extrudates were selected and their faces at both ends are sanded flat. Then specific cells were adapted.

## 2.2. Diffusion experiments

In this type of experiment, several extrudates impregnated with a high salt concentration (NaCl 2M) are placed in a basket with large mesh. At time  $t=0$ , this basket is introduced in a solution under stirring inside a thermoregulated cell. The mesh of the basket walls and the size of the extrudates are such that the flow of liquid is very fast in all the cell and around the extrudates so the concentration can be considered as constant in the whole system. In order to avoid the problems of surface charge, by screening the double layer, and the variation of diffusion coefficient with concentration, the solution in which the extrudates are immersed is itself highly concentrated. In the present case, extrudates impregnated with 2M NaCl are immersed in a 0.5M NaCl solution. In this concentration range the bulk diffusion coefficient of NaCl only varies a little:  $1.55 \pm 0.05 \cdot 10^{-9} \text{ m}^2\text{s}^{-1}$  [18,19]. For transverse diffusion, extrudates are used directly or after plugging their end with a small quantity of neoprene resin. Because side surface area of the cylinders is much higher than end surface area, results are similar. For longitudinal diffusion, a PTFE heat-shrink tube was used to eliminate release by side of the cylinder. The extrudate within the PTFE tube is heated in an oven with a temperature profile of 25 to 350 °C in one hour followed by another hour at 350 °C. Both ends of the assembly are then cut to get a precise dimension, around 10 mm. Their radius is around 0.9 mm. In all cases, the extrudates in their impregnation solution are evacuated a few minutes to improve the wetting. The conductivity of the solution is followed thanks to a standard conductivity cell and an impedancemetry apparatus (MODULAB XM ECS by Solartron Analytical, UK). This conductivity is proportional to the concentration in the narrow range of concentration variation considered here. It makes it possible to follow the concentration of the solution as a function of time thanks to a prior calibration. The main difficulty in this measurement, where the concentration of the solution varies very little between the start and the end of the experiment, around 1% because only a few extrudates are placed in a cell of around 30 mL, is the temperature stabilization which must be better than 0.01°C. From the evolution of concentration with time, it is possible to calculate the amount of solute that has been transferred from extrudate to solution through the surface. Practically, the following ratio is calculated:  $\frac{M(t)}{M(\infty)}$ .  $M(t)$  is the

quantity of solute that has crossed the surface of the cylinder at time  $t$  and  $M(\infty)$  this quantity after an infinite time. They are easily calculated experimentally from the concentrations measured as a function of time:  $M(t) = (C(t) - C(0)) * V$  where  $C(t)$  is the concentration in solution at time  $t$ ,  $C(0)$ , the initial one, and  $V$  the volume of solution. In the following two configurations are analyzed. In both cases the tortuosity is given by the ratio of the bulk diffusion coefficient to the efficient one in the porous medium (equation 3).

### 2.2.1 Longitudinal diffusion

In that configuration, the extrudates clad with their PTFE shrinkable polymer are used. Release of the NaCl occurs only by the ends of the cylinder. This configuration can be modeled by diffusion from an infinite slab of thickness  $L$ , the length of the cylinder, in which initial concentration is initially uniform and then varies with time, whereas the concentration at the outside surface is constant with time. Following Crank [20], the following equation can be applied:

$$\frac{M(t)}{M(\infty)} = 1 - \frac{8}{\pi^2} \sum_{n=0}^{\infty} \frac{1}{r(2n+1)^2} \cdot \exp(-D(2n+1)^2 \pi^2 t / L^2) \quad (4)$$

where  $r$  is the extrudate radius and  $D$  the efficient longitudinal diffusion coefficient. The fitting of experimental data by equation (4) enable the determination of  $D$ , which is the only unknown. Only the first 25 terms are considered in the right-hand side of equation (4) as no measure is done at very short times and convergence of the series is fast for enough long times. Tortuosity is then calculated by applying equation (3).

### 2.2.2 Radial diffusion

In that configuration, extrudates are directly used. A few experiments were done with extrudates having their end plugged by a small amount of resin but it does not change the result as expected from Watson *et al.* calculations [21], which show that the ratio of the contribution of the end of cylinders to the overall transfer is lower than the ratio of radius to length of the cylinder (less than 0.09 in the present case). This configuration can be modeled by diffusion from an infinite cylinder of radius  $r$  in which initial concentration is uniform and then varies with time, whereas the concentration at the outside surface is constant with time. The following equation can be applied [20]:

$$\frac{M(t)}{M(\infty)} = 1 - \sum_{n=1}^{\infty} \frac{4}{r^2 \cdot \alpha_n^2} \cdot \exp(-D \alpha_n^2 t) \quad (5)$$

where  $\alpha_n$  is such that  $r \cdot \alpha_n$  are the roots of:

$$J_0(r \cdot \alpha_n) = 0 \quad (6)$$

which are the roots of the zero order Bessel function. These roots are tabulated [20]. Again,  $D$ , here the efficient radial diffusion coefficient, is the only unknown and it can be deduced from the fitting of experimental data by equation (5). 12 terms are considered in the right-hand side of equation (5) for the same reason of fast convergence of the series for enough long times.

### 2.3. PFG-NMR

PFG-NMR was performed to measure the longitudinal tortuosity of monolith samples. The effective self-diffusion coefficient of toluene in an extrudate,  $D_{eff}$  was measured as well as the molecular diffusion coefficient,  $D_m$ , of toluene. Tortuosity  $\tau$  is calculated via equation (3) [10] since the diffusion is measured directly within the pores, the porosity is not considered.

The molecular diffusion coefficient measurement was done on a tube filled with 10% deuterated toluene. The deuterated fraction has the purpose of locking the NMR probe on the deuterium resonance frequency. For effective diffusion coefficient, the measure was repeated on three extrudates to consider the batch heterogeneity. Straight extrudates were fully immersed overnight in 10% deuterated toluene. Before measurement, one extrudate was removed from the vial, wiped with soft tissue to remove external toluene, and placed vertically in a 3 mm diameter tube that was sealed. Measurements were performed with a Bruker Avance 600 spectrometer (600 MHz resonance frequency for proton). Temperature was controlled during the experiments at 295 K. The echo attenuation coefficients were measured using the 13 interval Pulse Gradient Stimulated Echo Bipolar Pulse sequence [22] with a pulse gradient duration,  $\delta' = 0.6$  ms, a time between pulses,  $\Delta' = 136$  ms and inter-pulse separation,  $\tau' = 260$  ms. Magnetization wave vector space is probed by varying the intensity of the gradient  $g'$  (from about  $7 \times 10^{-3} \text{ Tm}^{-1}$  to  $3 \times 10^{-1} \text{ Tm}^{-1}$ ), in order to obtain 16 values of attenuation from 2% to 95%. The magnetic field gradient is on the vertical direction; thus the spin displacements are probed in the vertical and the transport along the longitudinal axis of the extrudate is measured. Plotting the logarithm of the attenuation versus  $(g'\gamma'\delta')^2 \times (4\Delta' + 6\tau' - 2\delta'/3)$ , where  $\gamma'$  is the gyromagnetic ratio of the nucleus, yields a line for small  $g'$  whose slope is the additive inverse of the diffusion coefficient (figure 1).

### 2.4. Chromatography

Chromatographic columns are prepared by placing in series, up to the desired column length, several straight extrudates. The faces at both ends of each extrudate are sanded flat to ensure they sit flush against one another. At either end of the extrudates stack, a short capillary HPLC fitting (i.d. 0.17 mm) is placed. The monoliths used in this study are of small diameter to avoid the use of extra fittings and connectors thus avoiding the introduction of high dead volumes into the system. A PTFE heat-shrink tube was used to secure the monoliths in place. With everything secured, the whole assembly is heated in an oven with a

temperature profile of 25 to 350°C in an hour followed by one hour at 350°C. A secondary, more rigid envelope is required to maintain the fittings with capillary. To this end, epoxy resin was set between the primary assembly and an outer plastic shell (EpoFix Resin from Struers), which ensured the mechanical resistance of the finished column (figure2).

An Agilent 1260 Infinity series HPLC was used, it is equipped with a high-performance degasser, a quaternary gradient pump, an automatic liquid sampler and a column compartment with thermostat (temperature fixed at 25°C). A variable wavelength detector is set to record the absorbance at 262 nm. The total extra-column volume in this system is  $87 \pm 2 \mu\text{L}$ . The ISEC, Inverse Size Exclusion Chromatography, and dynamic method experiments were performed according to Wernert et al. [23], using the same selection of probes. Toluene and a set of polystyrene, provided by Polymer Standard, were used as probes with various sizes. Solutions were prepared in THF, a solvent which ensures the experiments are performed in non-adsorbing condition [24]. The concentration and injection volume were chosen to generate a peak absorbance of around 100 mAu. All data on probe sizes and diffusion coefficients can be found in [23].

The method used here relies on the General Rate Model developed by Kucera et al. [25] as applied to the van Deemter equation. Mean retention time and variance, corrected from extracolumn dispersion, are extracted from chromatographic peaks taken at various velocities by fitting a Gaussian distribution. The height of an equivalent theoretical plate, HETP [26], is calculated with equation (7) where  $L$  refers to the length of the column,  $t_R$  and  $\sigma_R$  are the retention time and variance of the elution peak with column and  $t_i$  and  $\sigma_i$  are the same terms for an elution peak without column. This is done to eliminate the impact of the extra column volumes in the dispersion of the peak.

$$HETP = L \frac{\sigma_R^2 - \sigma_i^2}{(t_R - t_i)^2} \quad (7)$$

These HETP values are then plotted against linear velocity. The slope of the linear segment of the curve obtained should then be taken and the mesoporous diffusion coefficient,  $D_p^{eff}$ , is calculated using equation (8), the GRM for high enough velocities (linear regime), which is valid in non-adsorbing conditions

$$HETP \approx C \cdot u = 2 \frac{(1 - \varepsilon_e) \varepsilon_p [r_m]^2 \varepsilon_e}{\varepsilon_t [r_m]^2} \left[ \frac{d'_s}{4k_m} + \frac{d'_s{}^2}{32D_p^{eff} [r_m]} \right] \cdot u \quad (8)$$

$C$ , the diffusion parameter of the classic van Deemter is a function of the different porosity domains (external porosity,  $\varepsilon_e$ , mesoporosity,  $\varepsilon_p$ , and total porosity,  $\varepsilon_t$ ), the diameter of the skeleton of cylinders which comprises the structure of the monolith,  $d'_s$ , the mobile phase mass transfer coefficient,  $k_m$ , which is usually small enough to be negligible. Special attention must be paid to the porosity term and the

diffusion term, which vary with respect to the size of probe used to perform the experiment,  $r_m$ . The different factors used here are the result of the different topological characteristics of the monoliths, which approximates more closely to a labyrinth of cylindrical fibers, rather than the common assembly of spheres [27].

## 2.5. Electrical tortuosity measurements

Impedance spectroscopy measurements were performed by imposing an alternating current with a frequency range from 1 kHz to 1 MHz at a fixed voltage (30 mV). For all cases, the signal coming from the electrodes was processed with a Solartron Analytical Modulab XM ECS. Two configurations were used. The first one, for longitudinal tortuosity, is based on a column that is prepared with several extrudates. The second one uses a specific cell for transverse tortuosity.

### 2.5.1. Longitudinal tortuosity

The same column as that used for chromatographic experiment is filled with concentrated salt thanks to a high-pressure pump. Alligator clips are clamped to either end of the columns' metal fittings which function as electrodes, from which the resistance is measured. A blank column (with no monoliths) is used as a reference. Equation (9) gives us the total resistance,  $R$ , within a cylinder in the longitudinal direction, which is proportional to its length,  $L$ , and resistivity,  $\rho$ , and inversely proportional to its cross-sectional area,  $A$ .

$$R = \frac{\rho L}{A} \quad (9)$$

The blank column used had a smaller internal diameter than the monolithic column to ensure a snug fit of the capillary connectors. Measuring the resistance of the blank column  $R_0$ , and knowing its geometrical characteristics, one can calculate the resistivity of the blank system with the same diameter as the monolith. It is possible, then, to calculate the resistance of a blank with a cross-sectional area equal to the cross-sectional area of the monoliths. Given that resistivity is the reciprocal of conductivity, Equation (1) is easily adapted to the measurement of resistance.

$$\tau = \frac{R}{R_0} \varepsilon \quad (10)$$

### 2.5.2. Transverse tortuosity

Tortuosity was measured with an apparatus designed and built in-house. This apparatus has a chamber designed to hold the electrolyte and the sample. On either side of the chamber, cylindrical electrodes are axially centered and opposite each other. The distance between these electrodes can be adjusted with two micrometric control knobs to a precision of 1  $\mu\text{m}$ . The sample is kept in place with various PMMA plastic

support specifically designed to keep the monolith aligned with the center of the electrode within the electrolyte. A rectangular window is used to make transversal measurements. The extrudate is placed in the center of the window perpendicularly to the electrodes. Typically, the extrudate size is 0.9 mm radius and 10 mm length. It is placed vertically in the window with height  $H=9$  mm, thickness  $D=2.4$  mm and length  $L=2.4$  mm.  $L$  is the distance between electrodes. These values also define the dimensions of the conductivity cell. Measurements were performed with and without monolith in the cell to verify the resistivity of the liquid and then determine the bulk conductivity.

To mathematically solve the electrical problem, the method used in the literature [28,29] consists in solving the resistivity of an infinite assembly of cylinders, in a square array, with the same limit constraints in unit cell as in experimental conditions. These conditions are represented in figure 3. A composite made of two media is such defined: a cylinder of radius  $R$  and conductivity  $\sigma_{cylinder}$  surrounded by a liquid of conductivity  $\sigma^o$ . The Poisson equation, applied to the electrical potential  $V$ , should be verified for all values of  $r$  and  $\theta$  that are defined in figure 3:

$$\Delta V(r, \theta) = 0 \text{ for all } (r, \theta) \quad (11)$$

One defines a normalized conductivity:

$$\sigma = \frac{\sigma_{cylinder}}{\sigma^o} \quad (12)$$

The boundary conditions at the cylinder surface are:

$$\lim_{r \rightarrow R^-} (V(r, \theta)) = \lim_{r \rightarrow R^+} (V(r, \theta)) \quad (13)$$

$$\lim_{r \rightarrow R^-} \left( \sigma \frac{\partial V}{\partial r} \right) = \lim_{r \rightarrow R^+} \left( \frac{\partial V}{\partial r} \right) \quad (14)$$

The expression of the potential for  $r > R$  can be written under the form:

$$V(r, \theta) = A_0 + \sum_{n=1}^{\infty} \left( A_{2n-1} r^{2n-1} + \frac{B_{2n-1}}{r^{2n-1}} \right) \cos[(2n-1)\theta] \quad (15)$$

whereas for  $r < R$ , it is:

$$V(r, \theta) = C_0 + \sum_{n=1}^{\infty} C_{2n-1} r^{2n-1} \cos[(2n-1)\theta] \quad (16)$$

Applying the boundary conditions at the interface of the cylinder one gets:

$$A_{2n-1} = \left( \frac{1+\sigma}{1-\sigma} \right) \frac{B_{2n-1}}{R^{4n-2}} \quad (17)$$

$$C_{2n-1} = \left( \frac{2}{1-\sigma} \right) \frac{B_{2n-1}}{R^{4n-2}} \quad (18)$$

and from the Green theorem, the conductivity of the composite is given by:

$$\sigma_c = 1 - 2\pi B_1 \quad (19)$$

These equations are derived for the case where  $\sigma$  is larger than one, which is not the case here where the conductivity of the cylinder is smaller than that of the bulk liquid. Perrins et al. [30] showed that if the media are exchanged, the conductivity of the system is the reverse of that given by equation (19). Consequently, experimentally,  $\sigma_c$  and  $\sigma^o$  are determined. Then by using equations (14) to (18), a cylinder conductivity, quoted  $\sigma_{cylinder-test}$ , is calculated such that the  $\sigma_c$  value given by equation (19) is the reverse of the experimental one. The reverse of  $\sigma_{cylinder-test}$  gives the searched cylinder conductivity  $\sigma_{cylinder}$ . The tortuosity is then given by:

$$\tau = \frac{\varepsilon \sigma^o}{\sigma_{cylinder}} \quad (20)$$

where  $\varepsilon$  is the porosity of the extrudate. For the resolution of the various equations including a summation, the accuracy was good enough by considering  $n$  varying between 1 and 7. The solver of Excel is used by imposing that the potential is equal on ten points of the electrodes.

### 3. Results and Discussion

#### 3.1. Pore size characterization

Several methods were employed to measure and cross-check the pore size distribution of the alumina sample. The nitrogen adsorption isotherm and the pore size distribution calculated by the BJH method [5] are given in figure 4. This is a type IV adsorption-desorption isotherm showing the presence of mesopores. The saturation plateau at high relative pressure is not well defined, *i.e.* not horizontal. Such plateau is horizontal when the adsorption on the surface external to mesopores is negligible. This is not the case here because of the presence of macropores that are evidenced by mercury porosimetry, whereas the contribution of external surface of extrudates is negligible. The surface area of the sample determined by applying the BET method [5] is 220 m<sup>2</sup>g<sup>-1</sup>.

Intrusion-extrusion curves of mercury and corresponding pore size distributions are given in figure 5. They show that this sample presents two pore domains: one in the mesopore range and the other in the macropore range. When considering the mesoporous domain, below 50 nm, both mercury porosimetry and nitrogen adsorption show decent agreement between the measurements of the different porosity domain volumes and pore size distributions. Notably, the mesopore distribution present in both cases a main peak around 6 nm and a bump around 10 nm as already observed [4]. These distributions, also obtained on  $\gamma$ -alumina, are caused by the specific structural arrangement of the alumina crystals and crystal aggregates. The two independent yet overlapping pore domains correspond to intra-aggregate voids (between the alumina crystal platelets) and inter-aggregate voids. Both mercury and nitrogen adsorption measurements show a higher peak for the smaller mesopores domain. The macropore domain

evidenced by mercury porosimetry ranges between 0.2 and 1.5  $\mu\text{m}$ . Because the extrusion branch in the mesoporous domain does not come back on the intrusion branch before starting to empty macropores, it means that the meso and macro domain does not fill and empty independently. Some macropores are probably connected to the outside through mesopores.

In order to perform ISEC, which is another method to characterize pore size of materials, a very long column was used, such the volume explored is large enough to characterize the alumina sample accurately. The method enables the determination of the accessible porosity as a function of probe size as shown in figure 6. At low molecular weight, accessible porosity decreases, as expected, with an increase of probe size until a minimum when probes approach sizes comparable to the pore size, then an unexpected increase is observed. The nature of this hump in the graph is not immediately evident. However, given how the measurement is performed, some conjectures may be considered. Figure 6 shows that the external porosity, the one accessible to the largest probes, is severely overestimated in the ISEC measurements. Indeed, if only pores larger than 50 nm are considered, the macropore volume obtained for mercury is 0.30 mL/g, which corresponds to a porosity of 0.28 whereas the porosity accessible to the largest probes is 0.35, as seen by ISEC. The complete mercury porosimetry pore size distribution shows that the mesopores do not have a clear-cut upper limit, meaning that the monoliths display a complex array of features apart from the bimodal distribution of mesopores. Meso and macro domains are not clearly separated, neither in size nor in organization, as already stressed. It is then possible that, to enter in the macroporous domain 0.2-1.5  $\mu\text{m}$ , largest probes must go through pores that are not very large as compared to their own size. This may influence their apparent retention time, which is used to calculate the elution volume, leading to the apparent increase of accessible porosity evidenced in figure 5 for probes larger than 10 nm. Finally, the mesopore size distribution can also be obtained by ISEC: it is slightly shifted towards higher pore size as compared with nitrogen and mercury (figure 7) and does not provide as detailed distribution. Results of pore characterization are given in table 1.

All these results show a complex structure of the studied material. What are the consequences on its transport properties?

### **3.2 Transport properties**

Several methods were used here that give information on the transport behavior through the extrudate. One of them, chromatography, is a transport experiment that involves both advection and diffusion. The other experiments described in paragraph 2 are used to determine the tortuosity of the material: they involve only one phenomenon, diffusion or conductivity. Thanks to the specific shape of extrudates, it is possible to determine tortuosity in various configurations corresponding either to radial transport or longitudinal

transport. The results are given in table 2 where appear the analyzed phenomenon, the geometry type of transport, and the corresponding measured tortuosity.

Chromatographic approach enables also to access to the diffusion coefficient and then to the apparent tortuosity seen by a given probe. Nevertheless, to access to this diffusion coefficient, it is necessary to use a model, here the GRM detailed above, where contribution of advection and diffusion are separated. It is then supposed that advection occurs only in macropores, which means that at high velocity the HETP value is dominated by the C-term, equation (8), which is directly related to the diffusion in mesopores. This is why in table 2, the analyzed domain by method 4 is mesopores. For accuracy reasons, the dynamic conditions experiments are limited to mid-size probes, yet, useful information can still be retrieved from these data. The van Deemter plots for probes P4 through P7 show the typical positive slope (figure 8a), from which the general mesopore diffusion can be retrieved. Due to the inaccuracy of the HPLC pump at very low flow rates, values at flow rates below  $0.06 \text{ cm}\cdot\text{s}^{-1}$  fluctuate to some extent, however the curves fit the linear regime of the van Deemter plot soon after this limit. The efficient diffusion coefficient is then calculated from these fittings. In equation (8), the term containing the mobile phase mass transfer coefficient,  $k_m$ , is neglected.  $d'_s$ , represents the size of the skeleton of cylinders which comprises the structure of the extrudate. This is the solid porous region within which the mesopores reside and around which the macropores weave. In the case of the monoliths used, the size of the skeleton was measured by image analysis from scanning electron microscopy as being  $d'_s = 35.4 \text{ }\mu\text{m}$ . Using this value in the GRM, the diffusion coefficient within the mesopores,  $D_p^{\text{eff}}$ , for polymers of different sizes is finally calculated and plotted in figure 8b. These data could be used to calculate an apparent tortuosity for each probe in the mesoporous domain. To obtain an absolute tortuosity, it is necessary to extrapolate the data at zero probe size. In that aim, the calculation methods developed in references [23,31] are used. Briefly, the efficient diffusion coefficient in mesopores is expressed as a function of (i) accessible porosity calculated from probe size/pore size ratio, (ii) tortuosity of the porous network accessible to the probe calculated by a modified Weissberg equation [32] and (iii) friction effect calculated by Renkin equation [33].

$$\frac{D_p^{\text{eff}}[r_m]}{D_m} = \frac{\varepsilon_p[0](1-\lambda)^2(1-2.104\lambda+2.09\lambda^3-0.95\lambda^5)}{1-p \ln(\varepsilon_p[r_m])} \quad (21)$$

where  $\varepsilon_p[0]$  is the mesoporous volume from gas adsorption,  $\varepsilon_p[r_m]$  is the porosity accessible to the probe of radius  $r_m$ . The parameter  $p$  is used in the Weissberg equation as a fitting parameter of the variable tortuosity model. A value of  $p = 3.2$  was found to best fit the values. Extrapolating the model toward  $\lambda = 0$  (point-like probe), the effective diffusion coefficient is used now as an input to equation (2): a value of  $\tau_p = 2.66$  is obtained, corresponding to the mesoporous domain. PFG-NMR experiments with

toluene come interestingly close to this value, with  $\tau_p = 2.54$ . The domain probed by NMR is that of mesopores, since during the time of analysis the distance of diffusion is around 14  $\mu\text{m}$ , which is smaller than the mesoporous domains size quoted above. The other diffusion experiments to be compared are that of NaCl release. In such experiments, the diffusion in the whole extrudate is considered, whatever the porous domain. The difference with NMR and chromatography is that it is proposed here to analyze both longitudinal and transversal diffusion. Example of experiments are given in figure 9 for radial and longitudinal diffusion, respectively. The points correspond to experimental data and the lines to the models given by equation (5) and (4), for radial and longitudinal experiments, respectively. The residual noise on the signal corresponds to the temperature fluctuations, as stressed in the experimental part. The variation of concentration between the beginning and the end of the experiment is around 1%. The data are well fitted by the models in both cases. The efficient diffusion coefficients derived from this fitting procedure enable to calculate the tortuosities that are given in table 2. One can observe that longitudinal and transversal tortuosity obtained by these release experiments are different in the two directions, which let suppose an anisotropy in the extrudate. Looking now at the results of electrical measurements, the same observation can be done. The tortuosity deduced from transversal resistance measurement 2.75, is close to that of radial diffusion of NaCl, 2.85 whereas the longitudinal electrical tortuosity 2.45 is not very different from longitudinal diffusion. This anisotropy, weak but confirmed by several approaches, can be explained by the organization of the various porous domains. Looking at CT-SCAN and SEM images of figure 10, one can observe that some macropores are present in the longitudinal axis of the extrudate, whereas views on a radial section look more homogeneous. These macropores that can have a width of a few micrometer show lengths of several hundred  $\mu\text{m}$  in a direction parallel to the cylinder axis. From both radial and longitudinal images, they seem not connected to each other by other macropores, which agrees with our preceding remarks deduced from mercury porosimetry and ISEC analysis. They are also responsible for the anisotropy of tortuosity determined by the different experimental methods proposed here.

#### **4. Concluding remarks**

When considering porous materials that are shaped under a specific form for a given application, anisotropy can be created by the synthesis procedure. This anisotropy may have consequences, as observed here, on the transport properties. To evidence such anisotropy, several methods are proposed here. The simplest one seems to be the release of probes, here a salt, in controlled geometry. It needs only very simple laboratory equipment, excepted here a good temperature control because conductivity is used as concentration detector, and can be applied to any material. Electrical measurements are also simple in principle but limited to aqueous solutions and also to pore size ranges where the double layer can be

screened. NMR is a very powerful tool, but the porous domain that is analyzed is always under question. Finally, approaches such as band spreading analysis of chromatographic peak are also interesting in their ability to explore various pore domains by changing probe size, but a modeling is needed and the preparation of adapted column is sometimes itself a difficult task.

## References

- [1] H. Toulhoat, and P. Raybaud, *Catalysis by Transition Metal Sulphides - from Molecular Theory to Industrial Application*, Paris, Technip, 2013.
- [2] M. Marafi, H. Al-Sheeha, S. Al-Omani, and A. Al-Barood. "Activity of Hydroprocessing Catalysts Prepared by Reprocessing Spent Catalysts." *Fuel Processing Technology* 90 (2009) 264–69. <https://doi.org/10.1016/j.fuproc.2008.10.001>.
- [3] Y. M. Volfkovich, A. N. Fiipov and V. S. Bagotsky, *Structural Properties of Porous Materials and Powders Used in Different Fields of Science and Technology*, 2014.
- [4] S. Kolitcheff, E. Jolimaitre, A. Hugon, J. Verstraete, P.-L. Carrette, M. Tayakout-Fayolle, *Mic. Mes. Mat.* 248 (2017) 91-98. <http://dx.doi.org/10.1016/j.micromeso.2017.04.010>
- [5] F. Rouquerol, J. Rouquerol, K. S. W. Sing, P. Llewellyn, and G. Maurin, *Adsorption by Powders and Porous Solids*, 2nd ed. Academic Press, 2012.
- [6] M. Ben Clennell, *Geol. Soc. Lond. Spec. Publ.* 122 (1997) 299–344. doi:10.1144/GSL.SP.1997.122.01.18
- [7] S. J. Reich, A. Svidrytski, D. Hlushkou, D. Stoeckel, Ch. Kübel, A. Höltzel, U. Tallarek, *Ind. Eng. Chem. Res.* 57 (2018) 3031–3042. <https://doi-org.lama.univ-amu.fr/10.1021/acs.iecr.7b04840>
- [8] S. J. Reich, A. Svidrytski, A. Höltzel, W. Wang, Ch. Kübel, D. Hlushkou, U. Tallarek, *Mic. Mes. Mat.* 282 (2019) 188-196. <https://doi.org/10.1016/j.micromeso.2019.02.036>
- [9] D. Kondrashova, A. Lauerer, D. Mehlhorn, H. Jobic, A. Feldhoff, M. Thommes, D. Chakraborty, C. Gommers, J. Zecevic, P. de Jongh, A. Bunde, J. Kärger, R. Valiullin, *Sci. Rep.* 7 (2017) 40207; doi: 10.1038/srep40207
- [10] M.P. Hollewand, M. P., and L. F. Gladden, *Chemical Engineering Science*, 50 (1995) 309–26.
- [11] L.L. Latour, R.L. Kleinberg, P.P. Mitra, C.H. Sotak, *J. Magn. Reson., A* (1995), 83-91.
- [12] H. Chemmi, D. Petit, V. Tariel, J-P. Korb, R. Denoyel, R. Bouchet, and P. Levitz, *Eur. Phys. J. Special Topics* 224 (2015) 1749–1768.
- [13] M. Barrande, R. Bouchet, R. Denoyel, *Anal. Chem.*, 79 (2007) 9115.

- [14] R. Mesnier, Étude des liens entre la texture et les propriétés de diffusion de molécules modèles dans des milieux poreux bimodaux." Institut National Polytechnique de Toulouse, Thesis, 2008.<http://oatao.univ-toulouse.fr/7773/>.
- [15] E. Weiland, M. Springuel-Huet, A. Nossov, F. Guenneau, A. Quoineaud, and A. Gédéon, *New Journal of Chemistry* 40 2016, 4447–54. <https://doi.org/10.1039/C5NJ02952J>.
- [16] F. Gaulier, 2016. "Etude de la diffusion des charges lourdes en conditions réelles dans les catalyseurs d'hydrotraitement." Université Claude Bernard Lyon 1, Thesis
- [17] B. McEnaney and T.J. Mays, *Studies in Surface Science and Catalysis* 87 (1994) 327-337.
- [18] V. Vitagliano and P. A. Lyons, *J. Am. Soc.*, 78 (1956) 1549-1552.
- [19] J. A. Rard ' and D.G. Miller, *Journal of Solution Chemistry*, 8 (1979) 701-716.
- [20] J. Crank, *The Mathematics of Diffusion*. Clarendon Press, Oxford, 1975.
- [21] E. Bruce Watson, K. H. Wanser, K. A. Farley, *Geochimica et Cosmochimica Acta* 74 (2010) 614–633.
- [22] R. Cotts, M. Hoch, T. Sun, J. Marker, *Journal of Magnetic Resonance* 83 (1989) 252–266  
[https://doi.org/10.1016/0022-2364\(89\)90189-3](https://doi.org/10.1016/0022-2364(89)90189-3).
- [23] K. Long Nguyen, V. Wernert, A. Morgado Lopes, L. Sorbier, R. Denoyel, *Microporous and Mesoporous Materials* 293 (2020) 109776. <https://doi.org/10.1016/j.micromeso.2019.109776>
- [24] S. Mori, *Journal of Liquid Chromatography* 16 (1993) 1–13.  
<https://doi.org/10.1080/10826079308020892>.
- [25] E. Kučera, *Journal of Chromatography A* 19 (1965) 237–48.
- [26] , A. J. P. Martin and R. L. M. Synge, *Biochemical Journal*, 35 (1941) 1358.
- [27] K. Miyabe and G. Guiochon. 2002, *The Journal of Physical Chemistry B*, 106 (2002) 8898–8909.  
<https://doi.org/10.1021/jp020555b>
- [28] R.S. Lord Rayleigh, *Philosophical Magazine Series 5*, 34:211 (1892) 481-502.
- [29] W. T. Perrins, R. C. McPhedran and D. R. MCKenzie, *Thin Solid Films*, 57 (1979) 321-326.
- [30] W. T. Perrins, D. R. McKenzie and R. C. McPhedran, *Proc. R. Soc. Lond. A*, 369 (1979) 207-225.

doi: 10.1098/rspa.1979.0160

[31] V. Wernert, R. Bouchet, R. Denoyel, J. Chromatogr., A 1325 (2014) 179–185.

<https://doi.org/10.1016/j.chroma.2013.12.029>.

[32] H.L. Weissberg, J. Appl. Phys. 34 (1963) 2636–2639. <https://doi.org/10.1063/1.1729783>.

[33] E.M. Renkin, J. Gen. Physiol. 38 (1954) 225–2243.

#### Figure captions

Figure 1: logarithm of the attenuation versus  $(g'\gamma'\delta')^2 \times (4A' + 6\tau' - 2\delta'/3)$  for aliphatic protons.

Figure 2: Schema of finished column: green – PTFE liner; grey – HPLC capillaries; purple – plastic shell; lavender – epoxy resin; white rectangles – extrudates

Figure 3: representation of limit conditions for the conductivity cell.  $R$  is the radius of the cylinder.  $D$  is the width of the cell.  $L$  is the distance between electrodes that are placed at  $x=0$  and  $x=L$ .  $E_0$  is the electric field,  $V$ , the potential that depends on  $r$  and  $\theta$ . In  $y=0$  and  $y=D$  are placed non-conductive walls. The axis of the cylinder, direction  $z$ , is perpendicular to the figure.

Figure 4: nitrogen adsorption-desorption isotherm on the extrudates (left) and pore size distribution by BJH method applied to the desorption branch (right).

Figure 5: two cycles of mercury porosimetry intrusion-extrusion (left). Circles and squares correspond to first and second cycle, respectively. Pore size distribution calculated on the first intrusion branch(right).

Figure 6: accessible porosity versus probe size as determined by ISEC.

Figure 7: mesopore size differential distributions obtained by ISEC (triangles), N<sub>2</sub> adsorption (circles) and Hg porosimetry (squares).

Figure 8: a) HETP vs. linear velocity; b) effective diffusion coefficients versus probe/pore size ratio obtained by analysis of band spreading: experimental points and fitting by equation (21).

Figure 9: fraction of solute that has left the extrudate as a function of time: longitudinal diffusion (left) and radial diffusion (right). Points are experimental data. Lines correspond to equation (4) (left) and (5) right.

Figure 10: a) SEM images : top section view (left) and side section view (right) of extrudates at various magnifications. b) Microscanner images: top section view (left) and side section view (right) of extrudates

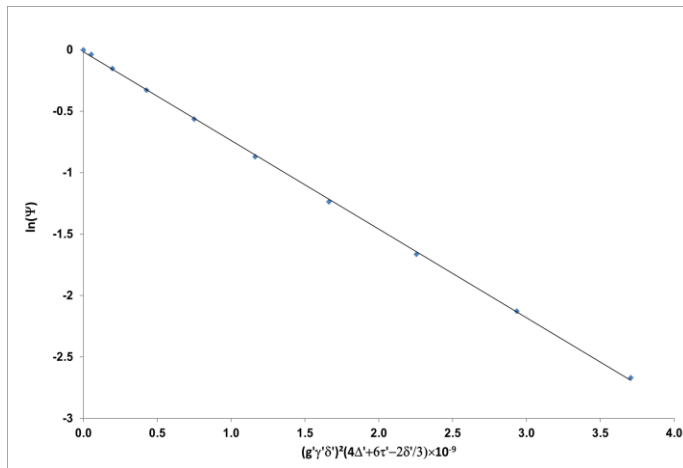


Figure 1: logarithm of the attenuation versus  $(g' \gamma' \delta')^2 \times (4A' + 6\tau' - 2\delta'/3)$  for aliphatic protons.

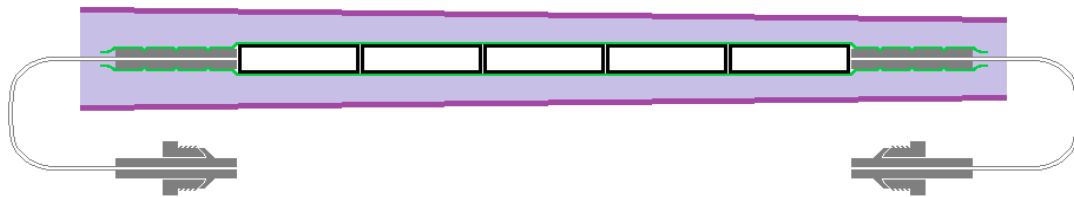


Figure 2: Schema of finished column: green – PTFE liner; grey – HPLC capillaries; purple – plastic shell; lavender – epoxy resin; white rectangles – extrudates

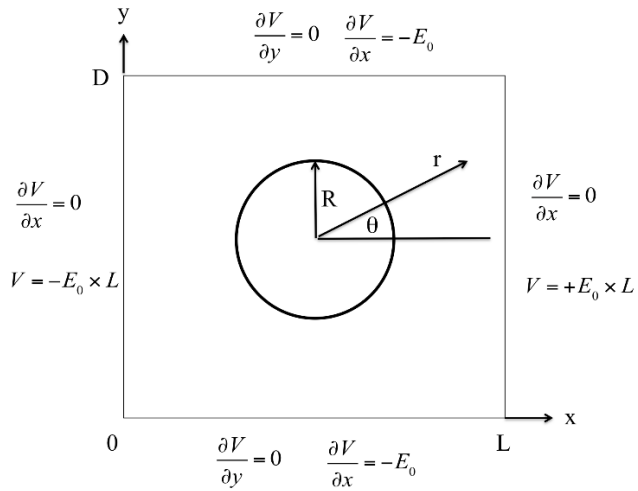


Figure 3: representation of limit conditions for the conductivity cell for transverse measurements.  $R$  is the radius of the cylinder;  $D=L$ .  $L$  is also the distance between electrodes that are placed at  $x=0$  and  $x=L$ .  $E_0$  is the electric field,  $V$ , the potential. In  $y=0$  and  $y=D$  are placed non-conductive walls. The axis of the cylinder, direction  $z$ , is perpendicular to the figure.

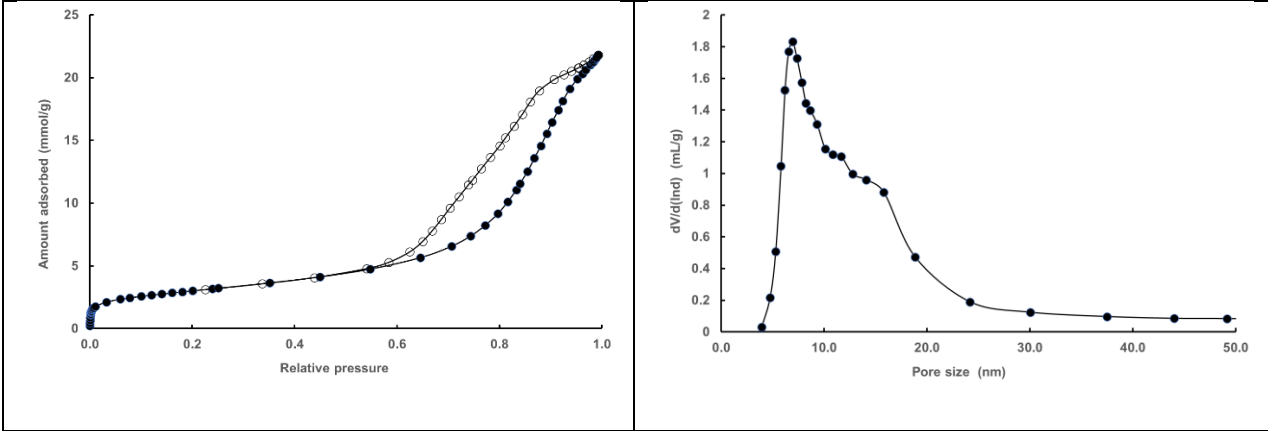


Figure 4: nitrogen adsorption-desorption isotherm on the extrudates (left) and pore size distribution by BJH method applied to the desorption branch (right).

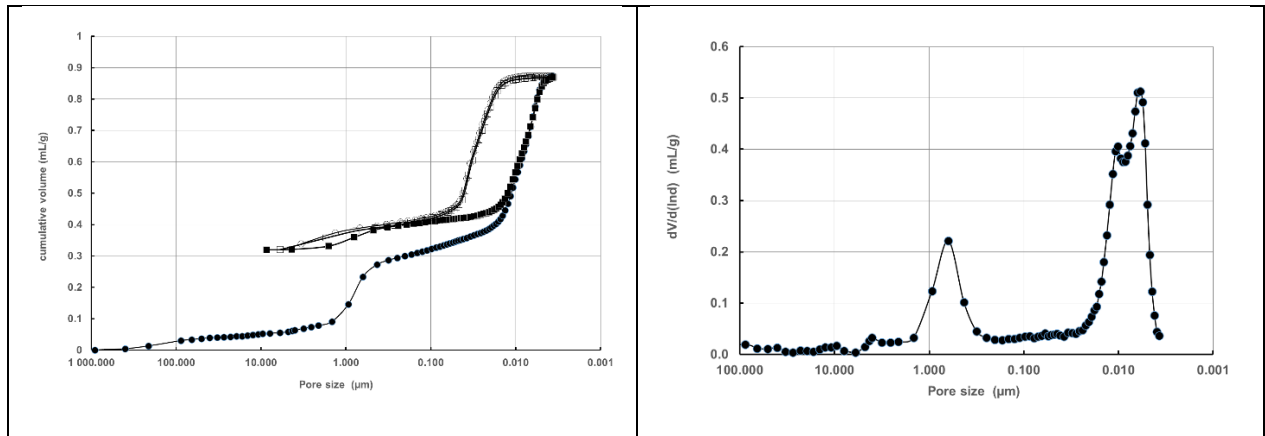


Figure 5: two cycles of mercury porosimetry intrusion-extrusion (left). Circles and squares correspond to first and second cycle, respectively. Pore size distribution calculated on the first intrusion branch(right).

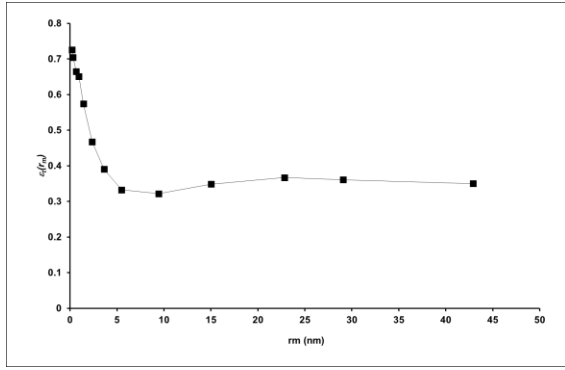


Figure 6: total accessible porosity  $\epsilon_t(r_m)$  versus probe size  $r_m$  as determined by ISEC.

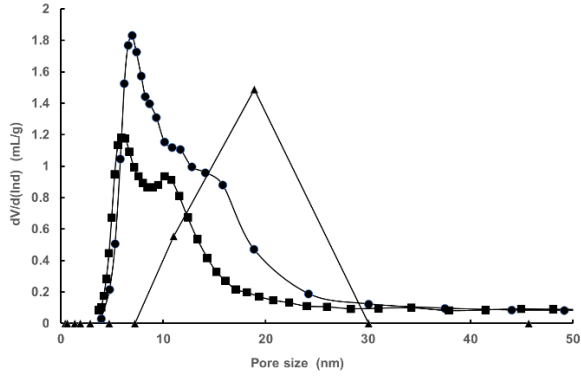
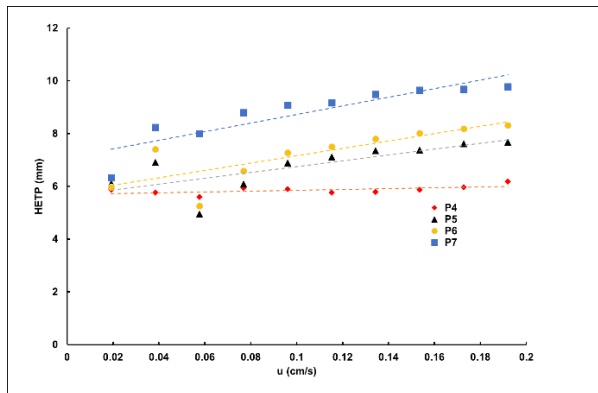


Figure 7: mesopore size differential distributions obtained by ISEC (triangles), N<sub>2</sub> adsorption (circles) and Hg porosimetry (squares).

a)



b)

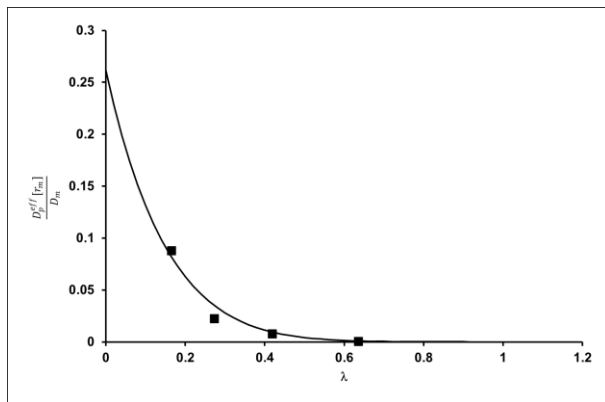


Figure 8: a) HETP vs. linear velocity; b) effective diffusion coefficient, normalized by bulk diffusion coefficient, is plotted versus probe/pore size ratio obtained by analysis of band spreading: experimental points and fitting by equation (21).

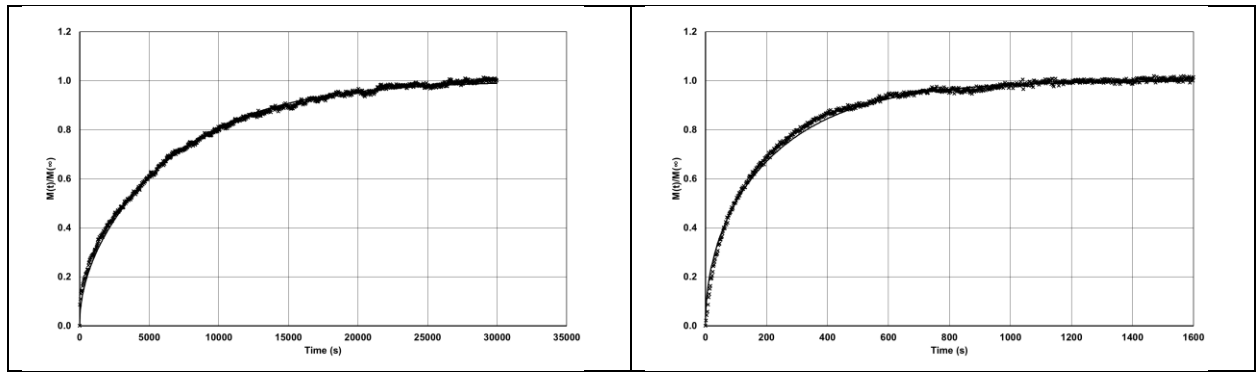
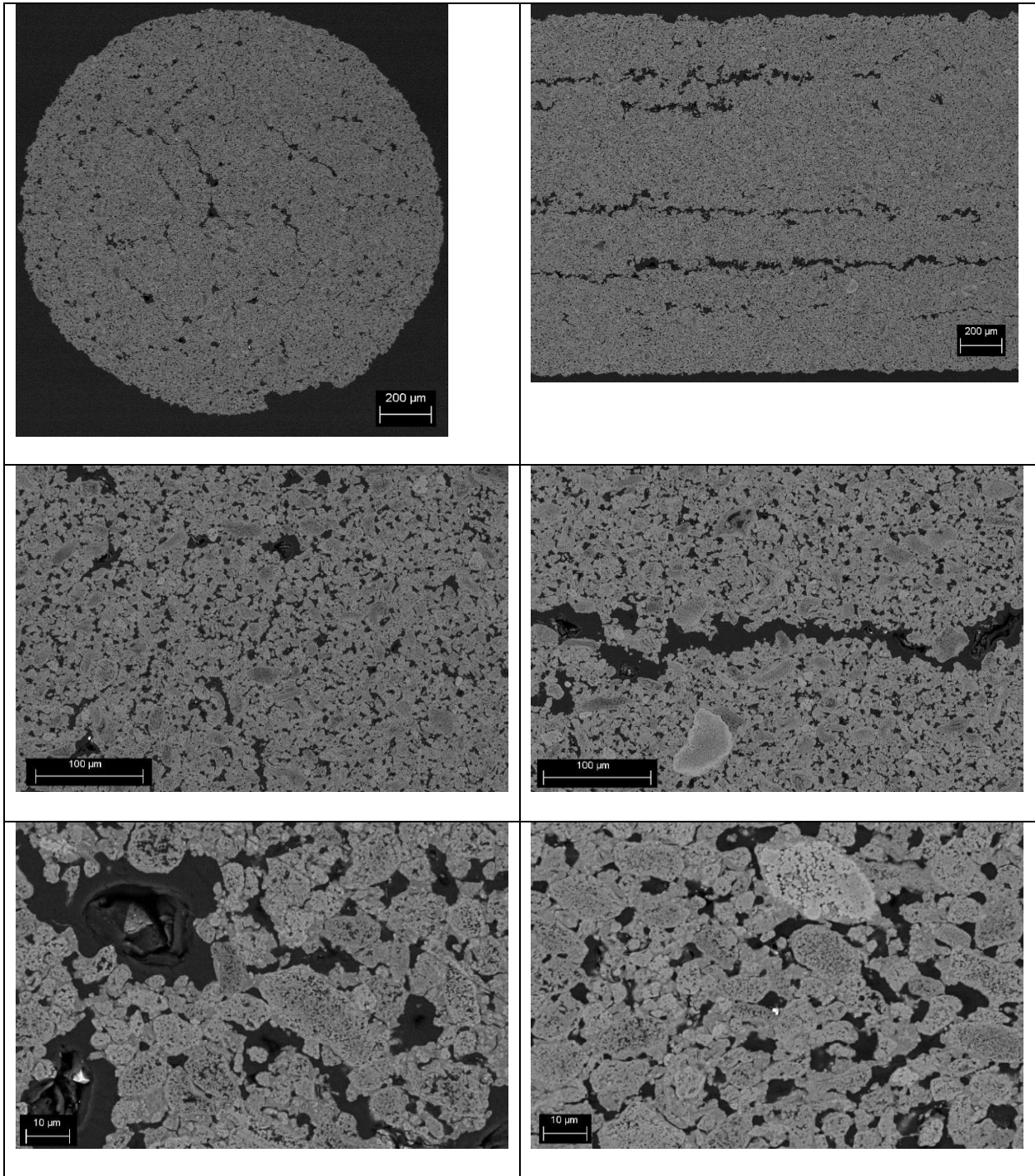


Figure 9: fraction of solute that has left the extrudate as a function of time: longitudinal diffusion (left) and radial diffusion (right). Points are experimental data. Lines correspond to equation (4) (left) and (5) right.

a)



b)

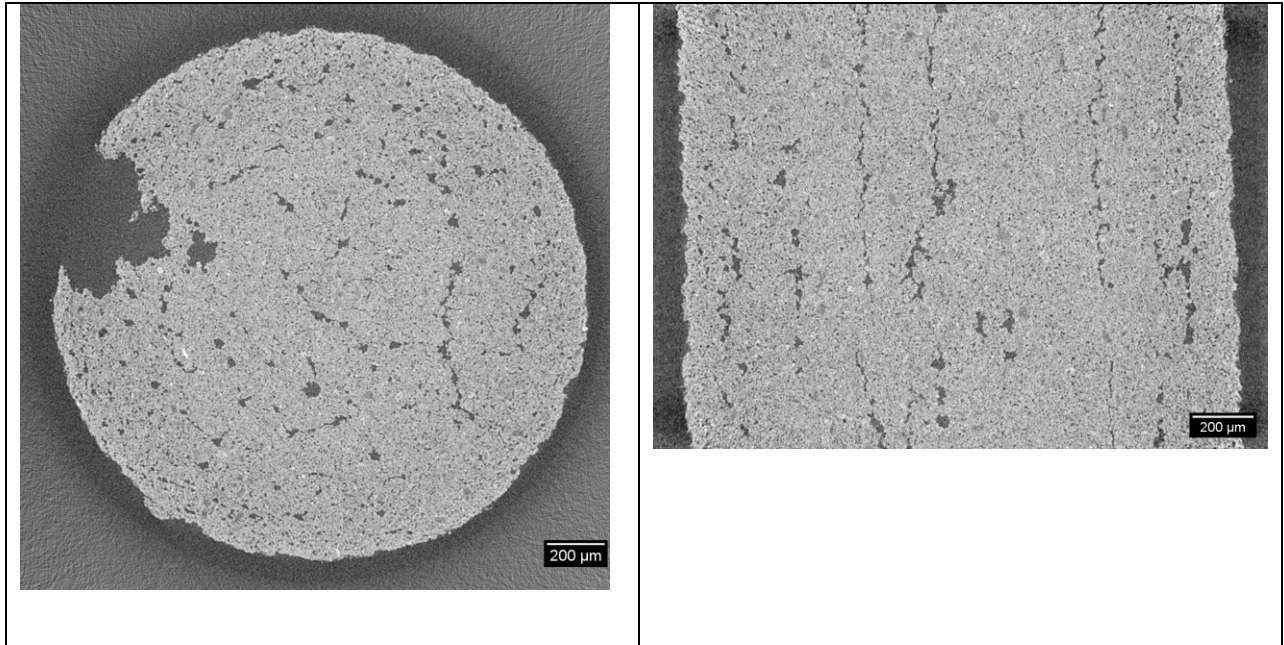


Figure 10: a) SEM images : top section view (left) and side section view (right) of extrudates at various magnifications. b) Microscanner images: top section view (left) and side section view (right) of extrudates

Table 1 – material structure parameters obtained by mercury porosimetry, nitrogen adsorption or ISEC.  
Quoted pore sizes correspond to the main peaks.

Method	Hg	N <sub>2</sub>	ISEC
Total pore volume / mL.g <sup>-1</sup>	0.92	-	0.91
Mesoporous volume / mL.g <sup>-1</sup>	0.56	0.67	0.47
Macroporous volume / mL.g <sup>-1</sup>	0.30	-	0.44
Mesopore size / nm	6 and 10	7 and 12	17
Macropore size/nm	630	-	-
S <sub>BET</sub> / m <sup>2</sup> .g <sup>-1</sup>	-	220	-

Table 2: tortuosity values

Method	Phenomenon	Tortuosity ±0.1	Analyzed domain
1 NMR longitudinal	Diffusion	2.54	Meso
2 NaCl release longitudinal	Diffusion	2.2	Meso+macro
3 NaCl release transversal	Diffusion	2.85	Meso+macro
4 Chromatography	Diffusion	2.66	Meso
5 Longitudinal resistance	Conductivity	2.39	Meso+macro
6 Transversal resistance	Conductivity	2.75	Meso+macro